minerals

Article

The Viscosity and Atomic Structure of Volatile-Bearing Melilititic Melts at High Pressure and Temperature and the Transport of Deep Carbon

Vincenzo Stagno [1,2,*], Veronica Stopponi [1], Yoshio Kono [3], Annalisa D'Arco [4], Stefano Lupi [4,5], Claudia Romano [6], Brent T. Poe [7], Dionysis I. Foustoukos [8], Piergiorgio Scarlato [2] and Craig E. Manning [9]

[1] Department of Earth Sciences, Sapienza University of Rome, 00185 Rome, Italy; veronica.stopponi@uniroma1.it
[2] National Institute of Geophysics and Volcanology, 00143 Rome, Italy; piergiorgio.scarlato@ingv.it
[3] Geodynamics Research Center, Ehime University, 790-8577 Matsuyama, Japan; kono.yoshio.rj@ehime-u.ac.jp
[4] INFN National Institute of Nuclear Physics, 00185 Rome, Italy; annalisa.darco@roma1.infn.it (A.D.); stefano.lupi@roma1.infn.it (S.L.)
[5] CNR-IOM and Department of Physics, Sapienza University of Rome, 00185 Rome, Italy
[6] Department of Sciences, University of Studies Roma Tre, L.go San Leonardo Murialdo 1, 00146 Rome, Italy; claudia.romano@uniroma3.it
[7] Department of Engineering and Geology, University of Chieti-Pescara, 66013 Chieti Scalo, Italy; brent.poe@unich.it
[8] Geophysical Laboratory, Carnegie Institution of Washington, Washington, DC 20015, USA; dfoustoukos@ciw.edu
[9] Department of Earth, Planetary and Space Sciences, University of California, Los Angeles, CA 90095, USA; manning@epss.ucla.edu
* Correspondence: vincenzo.stagno@uniroma1.it

Received: 5 February 2020; Accepted: 14 March 2020; Published: 16 March 2020

Abstract: Understanding the viscosity of mantle-derived magmas is needed to model their migration mechanisms and ascent rate from the source rock to the surface. High pressure–temperature experimental data are now available on the viscosity of synthetic melts, pure carbonatitic to carbonate–silicate compositions, anhydrous basalts, dacites and rhyolites. However, the viscosity of volatile-bearing melilititic melts, among the most plausible carriers of deep carbon, has not been investigated. In this study, we experimentally determined the viscosity of synthetic liquids with ~31 and ~39 wt% SiO_2, 1.3 and 1.5 wt% CO_2 and 5.7 and 1 wt% H_2O, respectively, at pressures from 1 to 4.7 GPa and temperatures between 1265 and 1700 °C, using the falling-sphere technique combined with in situ X-ray radiography. Our results show viscosities between 0.1044 and 2.1221 Pa·s, with a clear dependence on temperature and SiO_2 content. The atomic structure of both melt compositions was also determined at high pressure and temperature, using in situ multi-angle energy-dispersive X-ray diffraction supported by ex situ microFTIR and microRaman spectroscopic measurements. Our results yield evidence that the T–T and T–O (T = Si,Al) interatomic distances of ultrabasic melts are higher than those for basaltic melts known from similar recent studies. Based on our experimental data, melilititic melts are expected to migrate at a rate ~from 2 to 57 km·yr^{-1} in the present-day or the Archaean mantle, respectively.

Keywords: viscosity; melt structure; high pressure; falling-sphere technique; ultrabasic melt; Paris–Edinburgh press; magma ascent rate; migration rate

1. Introduction

Experimental studies show that low-degree partial melting of volatile-bearing mantle rocks can produce CO_2-rich melts at near solidus conditions throughout the upper and lower mantle [1–3]. There is also experimental evidence for the origin of ultrabasic magmas at high P–T, with SiO_2 contents up to about 40 wt%, as a result of either extensive melting of carbonated peridotite (CaO-MgO-Al_2O_3-SiO_2 + CO_2; [4]) at pressure (P) between 2 and 4 GPa and temperature (T) > 1400 °C or melting of a pyrolite in the presence of H_2O and CO_2 [5] at P > 1 GPa T > ~1100 °C. These magmas were shown to crystallize SiO_2-undersaturated effusive rocks such as (olivine-)melilitites and (olivine-)nephelinites and are often associated with carbonatite and kimberlite rock complexes, thus playing a key role in the transport of C stored in depth [6]. Along the carbonatite–basalt join, these magmas can dissolve amounts of CO_2 up to about 10 wt% despite having larger melt fractions (> 0.1 wt%) than carbonatitic melts at conditions of low P and high T [7]. For this reason, it is likely that magmas formed at the Archaean hot mantle conditions at shallow depths and reduced redox conditions beneath mid-ocean ridges [8] were foiditic (i.e., SiO_2 < 41 wt%; [9]) in composition and acted as early carriers of CO_2 from the interior of Earth to the atmosphere. Furthermore, the association of foiditic rocks with carbonatites and diamantiferous kimberlites worldwide suggests a common origin between the ultrabasic magmas by melting of CO_2-bearing rocks at variable depths in the Earth’s mantle [6]. However, while the P–T conditions for the origin and stability of foiditic melts are well constrained, knowledge of the viscosity of these melts at conditions of the upper mantle is needed to model their mobility and ascent velocity. These parameters have been recently made available for pre-carbonate compositions, including calcite, dolomite and Na_2CO_3 [10–12], and more recently on carbonate–silicate melts with ~18 wt% SiO_2 [13].

In this study, we extend the knowledge of the rheology of CO_2-bearing silicate melts by investigating the viscosity of volatile-bearing melilititic melts with variable SiO_2 content of 31 and 39 wt%, respectively.

2. Materials and Methods

Two starting materials were employed in this study, FOID1 and FOID2 (see [14] for a general description of these natural rocks). These are melilitite–olivine-bearing rocks whose mineral assemblage has been shown to consist of olivine + melilite ± nepheline, haüyne, monticellite, phlogopite, calcite, perovskite, spinels and apatite [15]. Table 1 shows the bulk rock chemistry of these two starting materials, determined by using a Spectro-XEPOS benchtop X-ray Fluorescence EDS spectrometer (Geophysical Laboratory, Carnegie Institution of Washington, Washington, DC, USA). These two samples are characterized by 39.45 wt% SiO_2 and 6.91 wt% Na_2O + K_2O (sample FOID1), and ~31 wt% SiO_2 and 2.16 wt% Na_2O + K_2O (sample FOID2), on an average of 5 measurements. The H_2O content was determined by using a Thermo Quest Finnigan Delta^{Plus} XL mass spectrometer (IRMS) coupled to a Thermo Finnigan thermal conversion elemental analyzer (TC/EA) (Geophysical Laboratory, Carnegie Institution of Washington), and it resulted in concentrations of ~1 and 6 wt% in FOID1 and FOID2, respectively. Protocols for H_2O analysis by IRMS-TC/EA have been benchmarked with solid-state ^{1}H Nuclear Magnetic Resonance spectroscopy in hydrous alumino–silicate glasses [16]. Finally, the CO_2 content (1.42 and 1.60 wt% FOID1 and FOID2, respectively) was determined by infrared technique (Actlabs Company, Report no. A19-14431). Due to their chemical compositions, both samples can be classified as melilitites (Figure S1 in Supplemental Materials; [9]) and, therefore, can be considered analogues of mantle volatile-bearing ultrabasic melts [4,5].

Viscosity measurements were conducted on the powdered FOID1 and FOID2 samples by using the falling-sphere technique in a Paris–Edinburgh large-volume press. In situ unfocused white X-ray radiography was conducted at beamline 16BM-B of the Advanced Photon Source (Illinois, USA) equipped with a high-speed camera Photron FASTCAM SA3 [17,18].

Table 1. Chemical composition of the bulk rocks used as starting materials from XRF analyses.

Oxides/Samples	FOID1	FOID2
SiO_2	39.45(49)	30.99(21)
TiO_2	2.46(8)	2.31(2)
Al_2O_3	11.32(10)	7.43(2)
Fe_2O_3	9.96(49)	14.31(10)
MnO	0.16(1)	0.26
MgO	13.87(13)	12.32(7)
CaO	13.99(17)	27.77(27)
Na_2O	3.53(7)	0.43(4)
K_2O	3.38(3)	1.73(1)
P_2O_5	1.87(1)	1.84(1)
SO_3^{2-}	0.01	0.61(1)
Totals	100.00	100.00
CO_2	1.42	1.60
H_2O	1.03(10)	5.73(23)

Notes: the volatile content (CO_2 and H_2O) is added to the normalized major elements analyses used for classification in Figure S1. The analytical standard deviation (1σ) is reported in terms of least units cited in parentheses.

The starting material was powdered and placed in a cylindrical graphite capsule with an inner diameter of 1.2 mm and height of 2 mm. Eight experiments were performed, with 3 runs using FOID1, and 5 runs with FOID2, at pressures between 1 and 4.7 GPa and temperatures between 1265 and 1755 °C (Table 2). Pt spheres prepared by arc melting, with a diameter between 85 and 146 μm, were placed in the upper portion of each capsule. One run was performed by using two Pt spheres, with one placed at the axial center and the other closer to the edge of the graphite capsule (run at 1.7 GPa/1265 °C), to quantify possible wall effects. Details on the cell assembly used in this study are available in Reference [17] and are the same as those used by Stagno et al. [12,13]. The pressure was monitored by collecting diffraction patterns on the MgO sleeve surrounding the graphite capsule and using the equation of state of MgO (EOS; [19]) on (111), (200) and (220) diffraction peaks. After compression to the target pressure, the temperature was set slowly up to about 200 °C below the melting T by using the power vs. temperature calibration curve corrected for the proper hydraulic pressure [17], and then quickly, until descent of the Pt sphere was observed.

The Pt sphere begins its descent once the material is totally molten, i.e. above its liquidus temperature. The trajectory of the falling Pt sphere was recorded at 125–500 frames per second (f.p.s.; see Table 2 and Figure S2). The image resolution of the ultrafast camera used for the viscosity measurements was 2.5 μm/pixel. The radiographic images were used to calculate the velocity of the sphere at each corresponding position along the descent path, in order to determine its terminal velocity (Figures S3–S18) by using the Tracker plugin in the ImageJ software [20]. From the velocity of the falling sphere(s), the melt viscosity is calculated by using the Stokes equation:

$$\eta = \frac{gd^2(\rho_s - \rho_l)}{18\upsilon}\frac{F}{E} \tag{1}$$

where ν is the terminal velocity (mm/s); ρ_s and ρ_l are the densities (g/cm^3) of the Pt sphere (~19.3 g·cm^{-3} as calculated from the thermal equation of state; [21]) and melt, respectively; and d is the diameter of the sphere (mm) determined from the radiographic images, using the Prosilica GC1380 high-resolution camera with pixel size of 0.945 μm/pixel (except for the runs at 1.7 GPa/1265 °C and 4.2 GPa/1700 °C, with a resolution of 0.851 μm/pixel). E and F are correction factors for the wall- and end- effects, respectively. A fixed value of 2.5 g·cm^{-3} was chosen for the density of our ultrabasic melts (ρ_l). This value is a midpoint between the density of 2.3 g·cm^{-3} estimated for carbonate–silicate liquids [22] and about 2.7 g·cm^{-3} measured for basalts [23] within a similar P–T range of our experiments. Despite the relative uncertainty of the melt density, the uncertainty in viscosity can be minimized by our choice of the much denser Pt as sphere, such that relative uncertainty of the density difference between sphere and liquid ($\rho_s - \rho_l$, Equation (1)) remains small. After the fall of the Pt sphere, as shown in Figure 1, the experiments were terminated by shutting down the power to the furnace in order to instantaneously quench the sample. In three of the runs, however, the melt structure was measured by multi-angle energy dispersive X-ray diffraction at high P–T [17]. These runs are listed in Table 3. For the runs with structure measurements, the sample remained molten for 3–4 h, and pressure was measured before and after the structure measurements. We collected X-ray diffraction patterns from the molten samples at 2θ angles of 3°, 4°, 5°, 7°, 9°, 12°, 16°, 22° and 28° (and 35° in case of run FOID1 at 4.2 GPa and 1700 °C). The slit sizes of the incident and diffracted X-rays were adjusted at every 2θ angle, to fix the Ge-SSD dead time at less than 15%. The background-subtracted EDXD data were analyzed by using a software package provided by the beamline (see Reference [17] for details). The recovered quenched samples were analyzed both for textural observations and chemical composition (Tables S1 and S2 in the Supplementary Materials), using the electron microprobe JEOL 8200 Superprobe available at the HPHT Laboratory of Experimental Volcanology and Geophysics of National Institute of Geophysics and Volcanology in Rome (Italy). Additional measurements on the recovered quenched products were conducted, using the Vector 22 Bruker interferometer, equipped with a broadband MCT detector and a Globar infrared source, coupled to a Hyperion 1000 infrared microscope available at the Physics Department of Sapienza University (Rome). The frequency resolved measurements cover the spectral region from 600 to 8000 cm^{-1}, with resolution of 2 cm^{-1} in reflection mode within selected areas from 50 × 50 to 200 × 200 μm. Raman spectra were acquired by using the Horiba LabRam HR 800 spectrometer at the Department of Science, Roma Tre University (Italy). Data were collected by using a 600 grooves/mm spectrometer grating and a CCD detector. A Nd-YAG laser at 532 nm (green laser) was used as the light source with 60 mW laser power, with a confocal hole of 300 μm, slit of 200 μm and an exposure time of 60 s. The Raman scattering was collected by a 100× objective and ~5 μm^2 spot size on the polished sample surface over a range from 200 to 4000 cm^{-1}. About four to five measurements were performed on each glass to verify its chemical homogeneity.

3. Results

3.1. Melt Viscosity

Results of our experiments are listed in Table 2.

Table 2. Experimental conditions and results.

Run	*P (GPa)	*T (°C)	ø Pt Sphere (mm)	Terminal Velocity (mm/s)	Recording Time (f.p.s.)	Viscosity (Pa·s)
FOID1_RUN1	2.5	1580	122	0.097(±0.007)	125	1.0855(±0.1441)
FOID1_RUN2	4.7	1755	121	0.441(±0.022)	500	0.2336(±0.0178)
FOID1_RUN3_2018	4.2	1700	85	0.089(±007)	500	0.6334(±0.0738)
FOID2_RUN1	1	1270	146	0.067(±0.007)	125	2.1221(±0.4253)
FOID2_RUN2	3.4	1360	142	0.225(±0.012)	250	0.6021(±0.3802)
FOID2_RUN3	4.5	1540	120	0.981(±0.093)	500	0.1044(±0.0320)
FOID2_2018 center bottom	1.7	1265	134	0.343(±0.013)	250	0.3526(±0.0136)
FOID2_2018 edge	1.7	1265	131	0.349(±0.012)	250	0.3374(±0.0168)

Note: * Typical uncertainties on pressure and temperature in the Paris–Edinburgh cell experiments are less than 0.4 GPa and 60 °C [17,24,25].

Figure 1a,b shows selected radiographic images of the Pt sphere descent as function of time in FOID1_RUN2 and FOID2_RUN2, respectively. Distance–time profiles for all viscosity measurements are available in the Supplementary Materials (Figures S3–S18). The calculated viscosity of FOID1 melts varies from a minimum value of 0.2336 Pa·s at 1755 °C and 4.7 GPa to a maximum value of 1.0855 Pa·s at 1580 °C and 2.5 GPa. FOID2 shows viscosities ranging from 0.1044 Pa·s at 4.5 GPa and 1540 °C to 2.1221 Pa·s at 1 GPa and 1270 °C (Figure 2). This last value is higher than expected and corresponds reasonably well to the viscosity at near-liquidus conditions, i.e., closer to the glass–liquid transition temperature (see Movie SM1 in Supplementary materials). In a laminar flow environment, the terminal velocity of a particle free to move under the effect of the gravitational force is maximum along the cylindrical axis and decreases as it approaches the cylindrical wall. The experiment at 1.7

GPa and 1265 °C (FOID2_2018) was performed by using two Pt spheres, one placed at the center and one near the edge of the capsule (i.e., closer to the graphite furnace), to quantify possible wall effects at high T. This experiment resulted in two very similar viscosities of 0.3526(136) and 0.3374(168) Pa·s, respectively, suggesting that possible wall effects are negligible at high temperature.

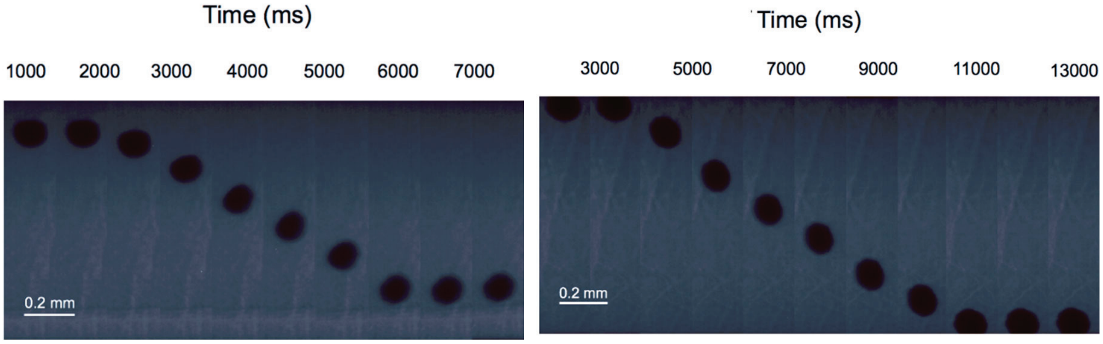

(a) (b)

Figure 1. X-ray radiography images of the Pt sphere falling in runs (**a**) FOID1_RUN2 (4.7 GPa/1755 °C) and (**b**) FOID2_RUN2 (3.4 GPa/1360 °C) as function of time.

3.2. *Effect of Pressure and Temperature on the Viscosity*

The viscosity data (Table 2) are shown as function of temperature (Figure 2a) and pressure (Figure 2b). The experimental data are compared to previous studies on the viscosity of pure carbonate melts and carbonated silicate melts. Our data range between 0.2336 and 1.0855 Pa·s for FOID1 and between 0.1044 and 2.1221 Pa·s for FOID2 and are, therefore, higher than those previously determined for carbonated melts within a similar temperature and pressure range. Figure 2a,b includes the viscosity of carbonated silicate melts performed on a $CaCO_3$–$CaSiO_3$ mixture with 22.6 and 31.4 wt% SiO_2, respectively [11], as well as data on transitional melts [13]. These experiments yielded viscosities near those resulting from our experiments at higher P and T. In case of FOID1, viscosities decrease with P and T, following a similar trend as that observed for carbonate–silicate melts. Both experimental [11–13] and theoretical [22] studies highlight the effect of temperature in lowering the viscosity of the melts. This effect is also observable in Figure 2a, where our data show a decrease in viscosity at increasing temperature by one order of magnitude. The runs using both FOID1 and FOID2 can be used to infer the effect of pressure, in particular those at 4.2 and 4.7 GPa at T of 1700 and 1755 °C, respectively. For runs using FOID2, those at 1 and 1.7 GPa at T of 1270 and 1265 °C show different viscosities that result from melting conditions near liquidus and well-above liquidus T, respectively. The effect of volatiles is expected to lower the viscosity of FOID2 more than FOID1, although a comparison with the viscosity of similar but anhydrous compositions would help to address the roles of H_2O and CO_2.

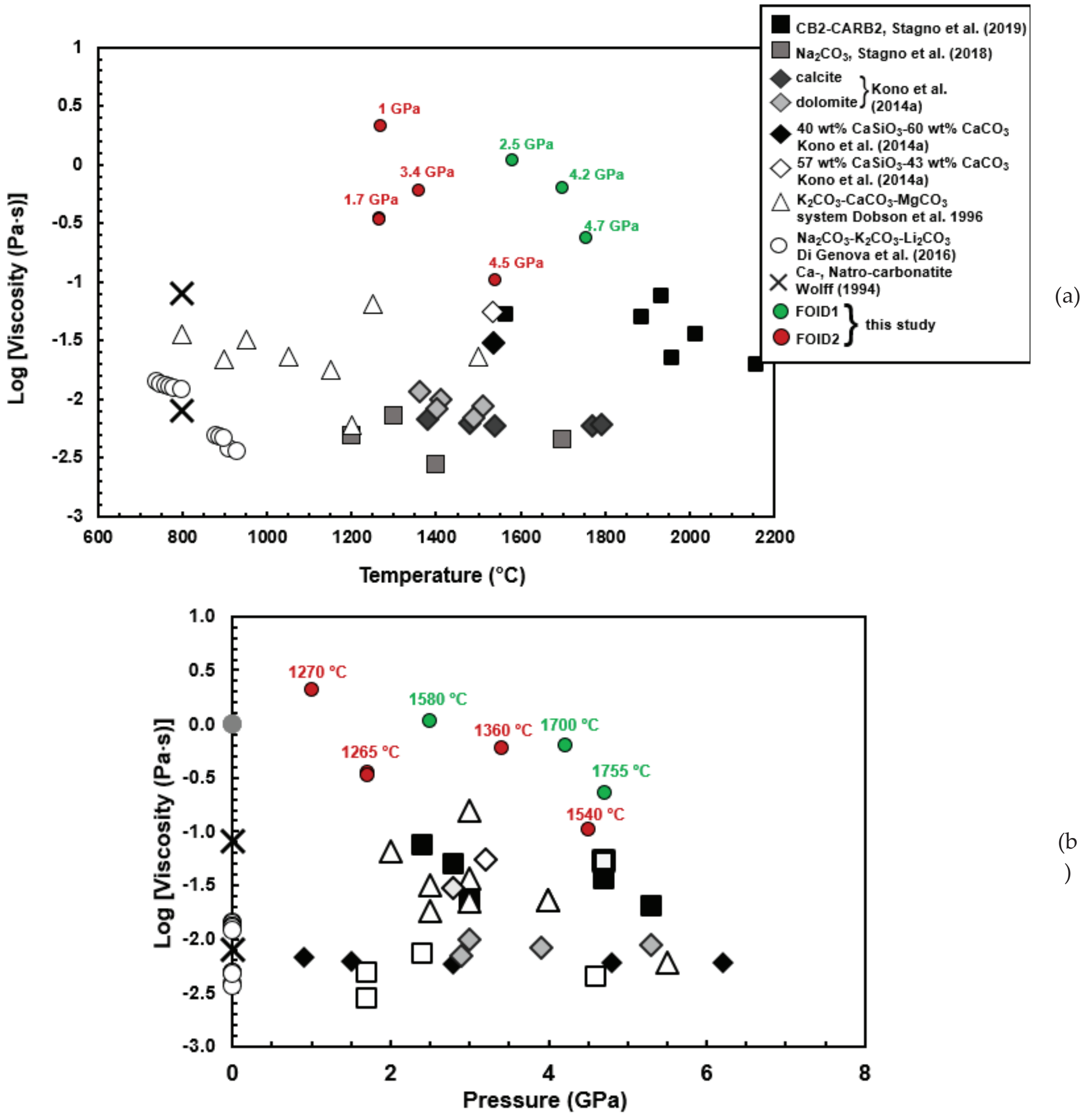

Figure 2. Shown are the obtained viscosity data plotted as a function of (**a**) temperature and (**b**) pressure. Data from literature are reported for comparison [10–13,26,27]. The uncertainty in our viscosity measurements is reported in Table 2.

3.3. Melt Structure Measurements

We collected X-ray diffraction patterns of FOID1 and FOID2 melts at conditions similar to those of the viscosity runs (Table 3). Prior to acquisition of the diffraction patterns, melting of the sample is verified by the vertical fall of the Pt sphere used to determine the viscosity and confirmed by the diffraction patterns collected before structure measurements (Figures S19–S21). These spectra show the presence of the liquid phase, although some diffraction peaks can be seen which correspond to the surrounding materials within the cell assembly. An EDXD pattern of the sample FOID2_RUN2 collected after the melt structure measurement and just before quench (Figure S20) shows peaks that are relative to either the surrounding cell material (graphite capsule) or olivine crystals. In contrast to our viscosity measurements at quite a short timescale (<10s), the melt structure measurements were made over a much longer timescale (3–4 h). The long duration may lead to (re)crystallization as result of P and/or T variations caused by softening of the cell (Table 3). In addition, C from the graphite capsule can oxidize to CO_2, with consequent dissolution into the melt. This could explain the low totals in Table S1. This process, and the crystallization of olivine, can explain the changes in the chemical composition observed from analysis of the recovered quenched glasses (Tables S1 and S2).

Nevertheless, the compositions fall within the field of melilitites, with the exception of FOID1_RUN3_2018 (nephelinite, Figure S1; [9]). Data-processing protocols are shown in Figures S22–S24. Figure 3 shows the interatomic distances determined by the pair distribution function G(r). From our results, the melt structures at high P–T are different between FOID1 and FOID2. The first sharp diffraction peak (FSDP) in the structure factor S(Q), which is related to the intermediate range order of the melt structure, is observed at ~2.16 Å^{-1} for FOID1_RUN3_2018 (Figure 3). In FOID_2 runs, the position of the FSDP appears at 2.18 Å^{-1} at 3.4 GPa/1360°C and 2.22 Å^{-1} at 4.5 GPa/1540 °C, showing a positive pressure dependence. These values are higher than both SiO_2 glass (1.5 Å^{-1}; [28,29]) and alkali basalts (~2 Å^{-1}; [30]), as it can be noted in Figure 3. Local structure in real space determined by the Fourier transformation of S(Q) gives T–O interatomic distance of 1.69 Å for FOID1_RUN3_2018, which is lower than in FOID2_RUN2 melt where the T–O is at 1.70 Å, then increasing to 1.73 Å at FOID2_RUN3, all reflecting the Si–O distance with fourfold coordination, as it has been shown at 1.63 Å for albite [31] and 1.62 Å for jadeite [32] liquids and at 1.59 Å in SiO_2 liquid [28]. The broadness and asymmetry of this peak suggests contribution from the Al–O bond [30]. The second peak appears in all runs between 2.27 and 2.40 Å and arises from the Ca–O correlation (~2.4 Å in haplogranitic melt, HPG; [24]). The second high-intensity peak at 3.20–3.26 Å can be assigned to the T–T interatomic distance and matches well with that observed at 3.2(3) Å in other studies (3.08 Å for albite liquids, [31]; 3 Å for basaltic liquids, [24,30]). Interestingly, the increase of the T–O distance for FOID2 indicates either an increase of the T–O–T angle or a change in the Si coordination [33,34].

Table 3. Experimental conditions of melt structure measurements.

Run	*$P_{initial}$ (GPa)	*P_{final} (GPa)	*$T_{initial}$ (°C)	*T_{final} (°C)	FSDP (Å^{-1})	T—O (Å)	M—O (Å)	T—T (Å)	Crystallized Minerals
FOID1_RUN3_2018	4.2	3.9^{+}	1700	1685	2.16	1.69	2.27	3.20	-
FOID2_RUN2	3.4	3.4	1360	1360	2.18	1.70	2.35	3.26	olivine
FOID2_RUN3	4.5	4.5	1540	1540	2.22	1.73	2.40	3.26	-

Note: * $P_{initial}$ and P_{final} refer to the pressure determined by the EoS of MgO before and just after the multi-angle X-ray diffraction measurement to determine the melt structure. + This P is determined by averaging the pressures obtained from the (220) and (200) diffraction peaks of MgO (4.1 and 3.7 GPa, respectively).

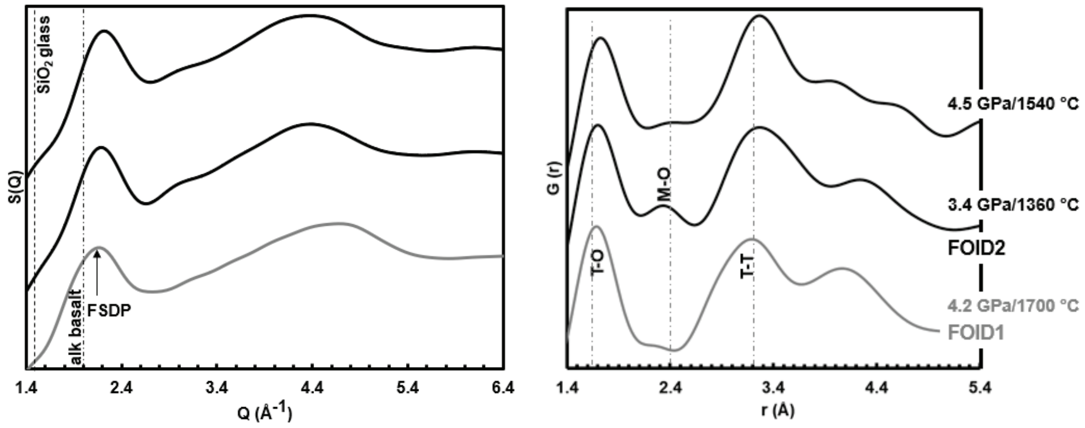

(a) (b)

Figure 3. (**a**) Structure factor, S(q), and (**b**) the reduced pair distribution function G(r) measured at high P–T, using the multi-angle energy-dispersive X-ray diffraction technique on FOID1 (gray line) and FOID2 (black line) compositions. Dashed lines are references for the known FSDP position and atomic distances from literature (see text).

3.4. Infrared Spectroscopy Measurements on Quenched Glasses

FTIR spectroscopic analyses were performed on samples quenched to glass at room temperature after the melt structure measurements (see Table 3) and the chemical composition of which is reported in Table S1. An additional quenched glass (FOID2_RUN1) was analyzed to investigate the possible effect of different P and T of quenching (1 GPa and 1270 °C; Table 1), where loss of CO_2 is expected [4,7]. We cannot exclude the presence of either un-melted or newly formed olivine crystals in some of our experiments, as suggested by EPMA analyses of the recovered quenched samples (FOID2_RUN1 and FOID2_RUN2 in Table S2) and supported by optical and back-scattered electron images (Figures S25–S28). However, despite the compositional shifts from the starting material, these glasses fall in the field of foidites for which spectroscopic measurements are useful and information is lacking in the literature. Samples embedded in resin epoxy were polished, and the reflectance was measured with respect to a silver mirror. The field-of-view of each analyzed sample was adjusted by closing variable rectangular apertures, placed between the objective (15×) and the MCT detector, along the optical path. Five spectra for each sample were collected by using 128 scans with a spectral resolution set at 2 cm^{-1}. To check potential influence of the aperture diameter on the spectra and the homogeneity of the samples, we varied the effective aperture diameter. Each fixed aperture was used to collect both sample and the background spectra. No difference was noted in the reflectance spectra. Figure 4 shows the infrared reflectance spectra of the recovered glasses dominated by three broad bands near 1000, 1300 and 1400 cm^{-1}, corresponding to the stretching modes of Si–O and carbonate species CO_3^{2-} according to King et al. [35], respectively. The shift of these bands to lower frequencies with respect to those reported in literature (pink shaded areas) indicates the more depolymerized structure of both quenched FOID1 and FOID2 glasses. A small sharp peak at ~2400 cm^{-1} can be associated with the presence of molecular CO_2 and seems to be more intense in the FOID2 spectra. On the other hand, chemical analyses of the glasses show quite low totals, suggesting that the concentration of CO_2 during the experiments increased likely due to oxidation of the surrounding graphite capsule. The negative slope at 3300–3600 cm^{-1} [35] characteristic of the O–H is only slightly visible in FOID2 runs, those having higher nominal water contents (Table 1). No effects referred to the different P–T of quench are observed between FOID2 compositions, excluding, therefore, the onset of decarbonation during the experiments.

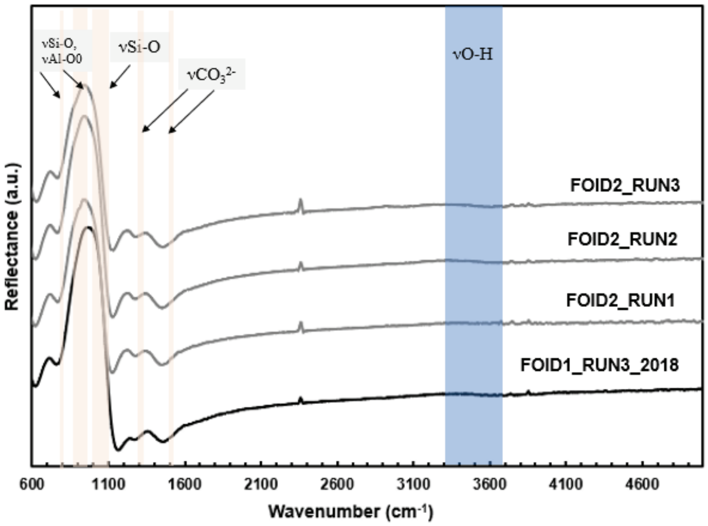

Figure 4. Background subtracted infrared reflectance spectra of the recovered glasses. The pink shaded areas are taken as reference by King et al. [35] for the Si–O and CO_3^{2-} bands. The blue shaded area refers to the frequency where a negative peak indicative of the presence water molecules is expected. Moreover, small peaks, appearing near to 3600 cm^{-1}, are due to atmospheric water vapor not fully compensated.

3.5. Micro-Raman Spectra of Quenched Glasses

Confocal micro-Raman spectra were obtained on the same glass samples that were analyzed by micro-FTIR recovered after the melt structure measurements. The spectra (Figure 5) are dominated by broad overlapping bands ranging from 700 to 1100 cm^{-1}, mostly due to T–O stretching vibrations of different Q^n-species distributed among SiO_4 and AlO_4 units. A weak feature appearing as a shoulder near 1060 cm^{-1}, however, is more likely to be due to the presence of CO_3^{2-} species, rather than any Q^4 species in these weakly polymerized glasses. At higher frequency, a broad peak is also observed near 1400 cm^{-1}, corresponding to the symmetric stretching vibration of dissolved molecular CO_2. This is more evident in FOID2 runs in agreement with that which was observed by FTIR (Figure 4). All glasses also show evidence of dissolved H_2O (Figure 5 inset) revealed by the asymmetric peak located near 3600 cm^{-1}. Raman spectra of the FOID2 glasses all contain narrow peaks near 200 and 280 cm^{-1} having the same relative intensity but different with respect to the broad bands belonging to the glassy portion of the spectrum. These peaks are clearly indicative of a nanocrystalline phase that formed during quench of this lower viscosity melt composition.

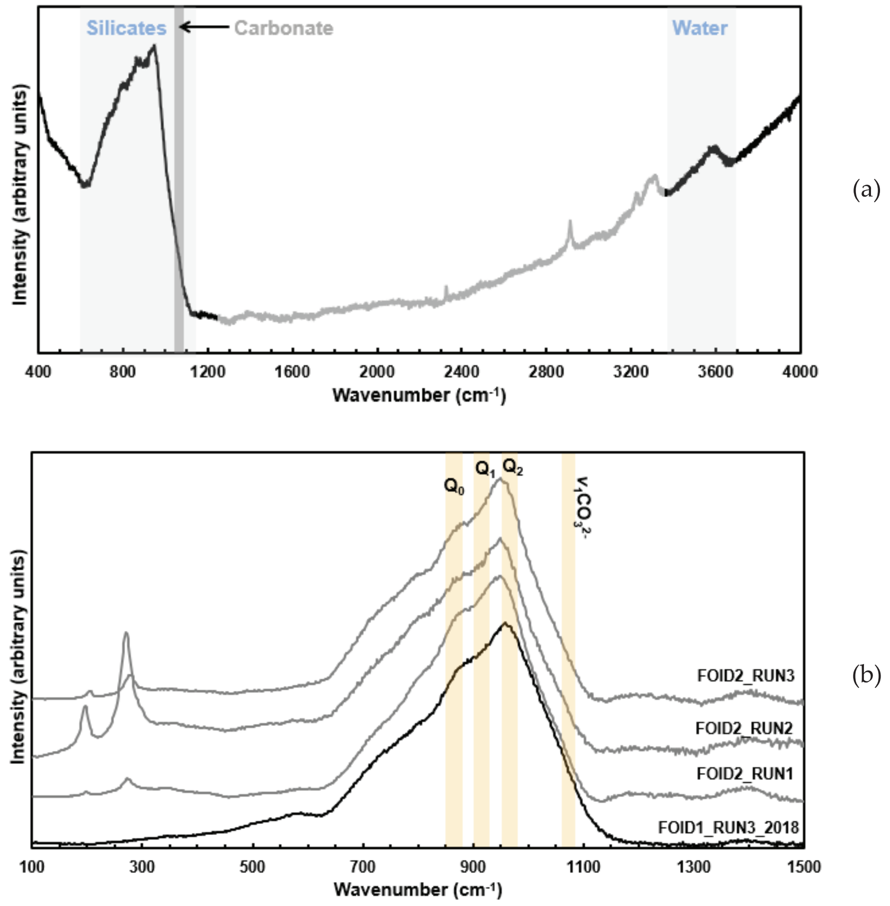

Figure 5. (**a**) Background subtracted Raman spectra of the recovered glasses in the Q^n and C–O frequency range. (**b**) Raw Raman spectrum of FOID2_RUN2 showing the silicate, CO_3^{2-} and O–H frequency intervals.

The spectra of our glasses are similar to those reported by Moussallam et al. [36] for low-SiO_2 compositions. Some of the glasses investigated by Moussallam et al. [36] are comparable to those of the present study in terms of SiO_2, Al_2O_3 and CO_2 content; however, some differences between our Raman spectra and those from their study are noted. First, a shoulder in the region between ~700 and 800 cm^{-1} is observed in our spectra that can be attributed to T–O (where T is Si and/or Al) stretching vibrations with a possible contribution also arising from TiO_2 in the glass (e.g., [37,38] and references therein). The presence of this shoulder cannot result from any method of baseline correction of the raw data (see inset in Figure 4). Additionally, in all of our spectra, a dominant broad peak is observed at ~950 cm^{-1}, whereas Moussallam et al. [36] observed the major contribution near ~880 cm^{-1} for SiO_2 contents between 30 and 40 wt% and $CO_2 < 2$ wt% that shifted to higher wavenumbers only for glasses with considerable amounts of CO_2 dissolved as CO_3^{2-} species, to suggest an increase in polymerization as more CO_{2tot} is present. Conversely, our FOID spectra appear more depolymerized with respect to those of both anhydrous and carbonate-bearing melilititic glasses investigated by Mysen and Virgo [39] and Sharma et al. [40], where an additional peak was observed at ~1010 cm^{-1}, attributed to the NBO/T = 1 structural unit.

4. Discussion

Melt Mobility and Ascent Rate of Volatile-Bearing Melilitic Magmas during the Archaean and Present-Day Earth's Upper Mantle

To date, determinations of the viscosities of CO_2-rich melts have mostly been limited to pure carbonate compositions chosen as analogues of natural carbonatitic melts. The viscosity was determined for Mg–K and Ca–K carbonate mixtures ([10]; viscosity (η) between 0.06 and 0.036 Pa·s), calcite and dolomite ([11]; η of 0.006–0.010 Pa·s and 0.008–0.010 Pa·s, respectively) and Na_2CO_3 ([12]; η of 0.003–0.007 Pa·s). More recently, Stagno et al. [13] conducted an experimental study on the viscosity of synthetic carbonate–silicate melt with ~18 wt% SiO_2 and ~22 wt% CO_2 as representative of natural transitional melts at pressures between 2.4 and 5.3 GPa and temperatures between 1565 and 2155 °C. Results ranged from 0.02 to 0.08 Pa·s and, when compared with previous results on molten carbonates mentioned above, provided the first experimental evidence of the effect of SiO_2 on the increase in viscosity. Here, we take an important step forward along the carbonatite–basalt join to provide insight into the time associated with the extraction of carbon from the Earth's interior via ultrabasic magmas. The viscosity in this study is determined at a T higher than that expected in the upper mantle (Table 2). In order to calculate the melt mobility and ascent rate of these melilitic magmas at a P–T relevant for the upper mantle, results can be fitted by using an Arrhenius-like equation, as reported by References [11,12] (see Equation (4) therein), for pure liquid carbonates taken as analogue of natural carbonatitic melts. With this aim, we apply the parameters $\eta_0 = 0.0531$ Pa·s, $Ea = 5318$ kJ·mol^{-1}, $V_a = 0.08$ cm^3·mol^{-1} and T_0 of 1370 K as best fitting to be used in order to scale our experimental data from FOID2 runs down to mantle P–T conditions. The ascent velocity, w_0, is calculated through the following equation:

$$\phi w_0 = \frac{kg\Delta\rho}{\eta} \quad (2)$$

where

$$k = \frac{a^2\phi^n}{C} \quad (3)$$

The permeability, k, depends on the characteristic mineral grain size, a, and the melt fraction, ϕ; and n and C are numerical constants equal to 2 and 3000, respectively. The permeability of the oceanic mantle links with the grain size that is a function of the thermal regime. Our calculations are performed at a depth of about 90 km at Ts of 1310 and 1450 °C to be representative of the present-day and Archaean T [2], implying a proposed grain size for the asthenospheric mantle of 5 and 15 mm, respectively [41,42]. For simplicity, the melt fraction is fixed at 1% [43] and the $\Delta\rho$ (density of the solid mantle density of pure carbonatitic melt) at 0.8 g·cm^{-3}. This leads to an average mobility, $\Delta\rho/\eta$, of volatile-bearing melilititic melts (e.g., FOID2) of 0.75 g·cm^{-3}·Pa^{-1}·s^{-1} (present-day mantle) and 2.46 g·cm^{-3}·Pa^{-1}·s^{-1} (Archaean upper mantle). The calculation using Equation (2) and Equation (3) results in the melt ascent velocity of ~1.9 km/yr and 57 km/yr, respectively, implying that, at the high thermal regime >3 Ga, the extraction of volatiles through mantle melting beneath mid-ocean ridges was more efficient than it is today. Similar calculations aimed at constraining the ascent rate of melilitic melts followed by their eruption in Archean cratons [6] requires a typical mineral grain size of about 7 mm, taken as the average observed in natural xenoliths [44,45], and a T regime of 1300 °C that results in an ascent velocity of 3–4 km/yr. This ascent rate is very close to that proposed for transitional melts [13] (~2 km/yr) and, along with similar estimates for carbonatitic melts [11,12], represents a reference value for better understanding the emplacement of the kimberlite-clan rocks as important carriers of carbon from the interior of Earth to the surface—either as CO_2 or as diamonds [46,47].

5. Conclusions

We determined that the viscosity of melilititic melts (~0.3–1 Pa·s) is higher than that recently proposed for carbonate–silicate melts within representative P–T conditions of the Earth's upper mantle. Recent studies point out the possibility that SiO_2 undersaturated magma might be invoked in early stage plate tectonics and be among the first melts to have extracted volatiles like water and CO_2 from the Archaean upper mantle. Our experimental results, combined with thermal and rheological parameters of mantle rocks, suggest a much slower ascent rate of melilititic melts compared to carbonatitic melts, but similar to that of carbonate–silicate melts. Finally, melt structure measurements confirm the comparatively unpolymerized nature of these liquids relative to basalts, as reflected in the greater T–O and T–T distances in melilititic liquids.

Supplementary Materials: The following are available online at www.mdpi.com/xxx/s1, File 1: Figures S1–S28 and Table S1, Video: SM1.

Author Contributions: V.S. (Vincenzo Stagno), C.E.M. and Y.K. conceived of the project; V.S. (Vincenzo Stagno) wrote the manuscript; V.S. (Vincenzo Stagno) and Y.K. performed melt viscosity and structure measurements; V.S. (Veronica Stopponi), A.D. and S.L. performed FTIR analyses; V.S. (Veronica Stopponi), C.R. and B.T.P performed Raman spectroscopy analyses; D.I.F. performed XRF analyses of the starting material; V.S. (Vincenzo Stagno), V.S. (Veronica Stopponi) and P.S. discussed the chemical data. All authors provided support in the data interpretation and revised the manuscript. All authors have read and agreed to the published version of the manuscript.

Funding: This research was funded by Sapienza University of Rome through Fondi di Ateneo 2016 and 2019 to V.Stagno and NSF-EAR-1761388 grant to Dionysis I. Foustoukos; Vincenzo Stagno also acknowledges financial support from the DeepCarbon Observatory (DCO). Portions of this work were performed at HPCAT (Sector 16), Advanced Photon Source (APS), Argonne National Laboratory. HPCAT operations are supported by DOE-NNSA's Office of Experimental Sciences. The Advanced Photon Source is a US Department of Energy (DOE) Office of Science User Facility operated for the DOE Office of Science by Argonne National Laboratory under Contract No. DE-AC02-06CH11357.

Acknowledgments: This manuscript benefited from thoughtful comments from Christelle Sanloup and two anonymous reviewers. Vincenzo Stagno is grateful to Michele Lustrino for providing the natural samples used in this study, and Manuela Nazzari for her assistance with the EPMA analyses at INGV (Rome).

Conflicts of Interest: The authors declare no conflict of interest.

References

1. Hammouda, T.; Keshav, S. Melting in the mantle in the presence of carbon: Review of experiments and discussion on the origin of carbonatites. *Chem. Geol.* **2015**, *418*, 171–188.
2. Stagno, V. Carbon, carbides, carbonates and carbonatitic melts in the Earth's interior. *J. Geol. Soc.* **2019**, doi:10.1144/jgs2018-095.
3. Stagno, V.; Cerantola, V.; Aulbach, S.; Lobanov, S.; McCammon, C.A.; Merlini, M. Carbon-bearing phases throughout Earth's interior—Evolution through space and time. In *Deep Carbon: Past to Present*; Orcutt, B., Daniel, I., Dasgupta, R., Eds.; Cambridge University Press: Cambridge, UK, 2019; pp. 66–88.
4. Gudfinnsson, G.H.; Presnall, D.C. Continuous gradations among primary kimberlitic, carbonatitic, melilititic, basaltic, picritic, and komatiitic melts in equilibrium with garnet lherzolite at 3–8 GPa. *J. Petrol.* **2005**, *46*, 1645–1659.
5. Wallace, M.E.; Green, D.H. An experimental determination of primary carbonatite magma composition. *Nature* **1988**, *335*, 343–346.

6. Woolley, A.R.; Kjarsgaard, B.A. Carbonatite occurrences of the world: Map and database. In *Geological Survey of Canada 2008, Open File 5796, 1 CD-ROM + 1 Map*; Natural Resources Canada: Ottawa, Canada, 2008.
7. Brey, G.; Green, D. Solubility of CO_2 in olivine melilitite at high-pressures and role of CO_2 in Earth's upper mantle. *Contrib. Mineral. Petrol.* **1976**, *55*, 217–230.
8. Aulbach, S., Stagno, V. Evidence for a reducing Archean ambient mantle and its effects on the carbon cycle. *Geology* **2016**, *44*, 751–754.
9. Le Bas, M.J. Nephelinitic and basanitic rocks. *J. Petrol.* **1989**, *30*, 1299–1312.
10. Dobson, D.P.; Jones, A.P.; Rabe, R.; Sekine, T.; Kurita, K.; Taniguchi, T.; Kondo, T.; Kato, T.; Shimomura, O.; Urakawa, S. In-situ measurement of viscosity and density of carbonate melts at high pressure. *Earth Planet. Sci. Lett.* **1996**, *143*, 207–215.
11. Kono, Y.; Kenney-Benson, C.; Hummer, D.; Ohfuji, H.; Park, C.; Shen, G.; Wang, Y.; Kavner, A.; Manning, C.E. Ultralow viscosity of carbonate melts at high pressures. *Nat. Commun.* **2014**, *5*, 5091.
12. Stagno, V.; Stopponi, V.; Kono, Y.; Manning, C.E.; Irifune, T. Experimental determination of the viscosity of Na_2CO_3 melt between 1.7 and 4.6 GPa at 1200–1700 °C: Implications for the rheology of carbonatite magmas in the Earth's upper mantle. *Chem. Geol.* **2018**, *501*, 19–25.
13. Stagno, V.; Kono, Y.; Stopponi, V.; Masotta, M.; Scarlato, P.; Manning, C.E. The viscosity of carbonate-silicate transitional melts at Earth's upper mantle pressures and temperatures, determined by the in situ falling-sphere technique. In *Carbon in Earth's Interior*; Manning, C.E., Lin, J., Mao, W., Eds.; Carbon in Earth's Interior, AGU Monographs; 2020, in press.
14. Stagno, V.; Luciani, N.; Narzisi, S.; Faraone, D.B.; Lustrino, M.; Masotta, M.; Scarlato, P. *Experimental Constraints on Limestone–Ultrabasic/Basic Melt Interaction at 2 Kbar. Basalt 2017*; Kadaň, Czech Republic, 18–22 September 2017. Available online: http://basalt2017.geocon.cz/Stagno.pdf (accessed on 16 March 2020).
15. Ulrych, J.; Adamovič; J.; Krmíček, L.; Ackerman, L.; Balogh, K. Revision of Scheumann's classification of melilitic lamprophyres and related melilitic rocks in light of new analytical data. *J. Geosci.* **2014**, *59*, 3–22, doi:10.3190/jgeosci.158.
16. Cody, G.D.; Ackerson, M.; Beaumont, C.; Foustoukos, D.I.; Le Losq, C.; Mysen, B.O. Water speciation in hydrous alumino-silicate glasses: Discrepancy between solid-state H NMR and NIR spectroscopy in the determination of X-OH and H_2O. *Geochim. Cosmochim. Acta* **2020**, in review.
17. Kono, Y.; Park, C.; Kenney-Benson, C.; Shen, G.; Wang, Y. Toward comprehensive studies of liquids at high pressures and high temperatures: Combined structure, elastic wave velocity, and viscosity measurements in the Paris- Edinburgh cell. *Phys. Earth Planet. Inter.* **2014**, *228*, 269–280.
18. Kono, Y. Viscosity measurement. In *Magmas under Pressure: Advances in High-Pressure Experiments on Structure and Properties of Melts*; Kono, Y., Sanloup, C., Eds.; Elsevier: Amsterdam, The Netherlands, 2018; pp. 261–280.
19. Kono, Y.; Irifune, T.; Higo, Y.; Inoue, T.; Barnhoorn, A. P-V-T relation of MgO derived by simultaneous elastic wave velocity and in situ X-ray measurements: A new pressure scale for the mantle transition region. *Phys. Earth Planet. Inter.* **2010**, *183*, 196–211.
20. Abramoff, M.D.; Magalhaes, P.J.; Ram, S.J. Image processing with ImageJ. *Biophotonics Int.* **2004**, *11*, 7, 36–42.
21. Dorogokupets, P.I.; Dewaele, A. Equations of state of MgO, Au, Pt, NaCl-B1, and NaCl-B2: Internally consistent high-temperature pressure scales. *High Press. Res.* **2007**, *27*, 431–446.
22. Ghosh, D.B.; Karki, B.B. Transport properties of carbonated silicate melt at high pressure. *Sci. Adv.* **2017**, *3*, e1701840.
23. Sakamaki, T.; Suzuki, A.; Terasaki, H.; Urakawa, S.; Katayama, Y.; Funakoshi, K.; Wang, Y.; Hernlund, J.W.; Ballmer, M.D. Ponded melt at the boundary between the lithosphere and asthenosphere. *Nat. Geosci.* **2013**, *6*, 1041–1044.
24. De Grouchy, C.J.L.; Sanloup, C.; Cochain, B.; Drewitt, J.W.E.; Kono, Y.; Crépisson, C. Lutetium incorporation in magmas at depth: Changes in melt local environment and the influence on partitioning behavior. *Earth Planet. Sci. Lett.* **2017**, *464*, 155–165.
25. Hudspeth, J.; Sanloup, C.; Kono, Y. Properties of molten $CaCO_3$ at high pressure. *Geochem. Perspect. Lett.* **2018**, *7*, 17–21.
26. Di Genova, D.; Cimarelli, C.; Hess, K.; Dingwell, D.B. An advanced rotational rheometer system for extremely fluid liquids up to 1273 K and applications to alkali carbonate melts. *Am. Mineral.* **2016**, *101*, 953–959.

27. Wolff, J.A. Physical properties of carbonatite magmas inferred from molten salt data, and application to extraction patterns from carbonatite–silicate magma chambers. *Geol. Mag.* **1994**, *131*, 145–153.
28. Funamori, N.; Yamamoto, S.; Yagi, T.; Kikegawa, T. Exploratory studies of silicate melt structure at high pressures and temperatures by in situ X-ray diffraction. *J. Geophys. Res.* **2004**, *109*, B03203.
29. Meade, C.; Hemley, R.J.; Mao, H.K. High-pressure x-ray diffraction of SiO_2 glass. *Phys. Rev. Lett.* **1992**, *69*, 1387–1390.
30. Crépisson, C.; Morard, G.; Bureau, H.; Prouteau, G.; Morizet, Y.; Petitgirard, S.; Sanloup, C. Magmas trapped at depth and the continental lithosphere-asthenosphere boundary. *Earth Planet. Sci. Lett.* **2014**, *393*, 105–112.
31. Yamada, A.; Wang, Y.; Inoue, T.; Yang, W.; Park, C.; Yu, T.; Shen, G. High-pressure X-ray diffraction studies on the structure of liquid silicate using a Paris–Edinburgh type large volume press. *Rev. Sci. Instrum.* **2011**, *82*, 015103.
32. Sakamaki, T.; Wang, Y.; Park, C.; Yu, T.; Shen, G. Structure of jadeite at high pressures up to 4.9 GPa. *J. Appl. Phys.* **2012**, *111*, 112623.
33. Sanloup, C.; Drewitt, J.W.E.; Kono^pková, Z.; Dalladay-Simpson, P.; Morton, D.M.; Rai, N.; van Westrenen, W.; Morgenroth, W. Structural change in molten basalt at deep mantle conditions. *Nature* **2013**, *503*, 104–107.
34. Drewitt, J.W.E.; Jahn, S.; Sanloup, C.; de Grouchy, C.; Garbarino, G.; Hennet, L. Development of chemical and topological structure in aluminosilicate liquids and glasses at high pressure. *J. Phys. Condens. Matter* **2015**, *27*, 105103.
35. King, P.L.; McMillan, P.F.; Moore, G. Infrared spectroscopy of silicate glasses with application to natural systems. In *Infrared Spectroscopy in Geochemistry, Exploration Geochemistry and Remote Sensing*; King, P.L., Ramsey, M.S., Swayze, G.A., Eds.; Short Course Series 2007; Mineralogical Association of Canada, Quebec City, QC, Canada: Volume 33, pp. 93–133.
36. Moussallam, Y.; Florian, P.; Corradini, D.; Morizet, Y.; Sator, N.; Vuilleumier, R.; Guillot, B.; Iacono-Marziano, G.; Schmidt, B.C.; Gaillard, F. The molecular structure of melts along the carbonatite–kimberlite–basalt compositional joint: CO_2 and polymerisation. *Earth Planet. Sci. Lett.* **2016**, *434*, 129–140.
37. Rossano, S.; Mysen, B.O. Chapter 9: Raman Spectroscopy of Silicate Glasses and Melts in Geological Systems. In *Raman Spectroscopy Applied to Earth Sciences and Cultural Heritage;* Dubessy, J., Caumon, M.-C., Rull, F.; EMU Notes in Mineralogy; European Mineralogical Union: Jena, Germany, 2012; Volume 12, pp. xvii + 504.
38. Yadav, A.K.; Singh, P. A review of structure of oxide glasses by Raman spectroscopy. *RSC Adv.* **2015**, *5*, 67583–67609.
39. Mysen, B.O.; Virgo, D. Solubility mechanisms of carbon dioxide in silicate melts: A Raman spectroscopic study. *Am. Mineral.* **1980**, *65*, 885–899.
40. Sharma, S.K.; Yoder, H.S., Jr.; Matson, D.W. Raman study of some melilites in crystalline and glassy states. *Geochim. Cosmochim. Acta* **1988**, *52*, 1961–1967.
41. Solomatov, V.S.; Reese, C.C. Grain size variations in the Earth's mantle and the evolution of primordial chemical heterogeneities. *J. Geophys. Res.* **2008**, *113*, B07408, doi:10.1029/2007JB005319.
42. Behn, M.D.; Hirth, G.; Elsenbeck, J.R., II. Implications of grain size evolution on the seismic structure of the oceanic upper mantle. *Earth Planet. Sci. Lett.* **2009**, *282*, 178–189, doi:10.1016/j.epsl.2009.03.014.
43. Dasgupta, R.; Mallik, A.; Tsuno, K.; Withers, A.C.; Hirth, G.; Hirschmann, M.M. Carbon-dioxide-rich silicate melt in the Earth's upper mantle. *Nature* **2013**, *493*, 211–215.
44. Avé Lallemant, H.G.; Mercier, J.-C.C.; Carter, N.L. Rheology of the upper mantle: Inference from peridotite xenoliths. *Tectonophysics* **1980**, *70*, 85–114.
45. Chu, X.; Korenaga, J. Olivine rheology, shear stress, and grain growth in the lithospheric mantle: Geological constraints from the Kaapvaal craton. *Earth Planet. Sci. Lett.* **2012**, *333–334*, 52–62, doi:10.1016/j.epsl.2012.04.019.

46. Haggerty, S.E. A diamond trilogy: Superplumes, supercontinents, and supernovae. *Science* **1999**, *285*, 851–860, doi:10.1126/science.285.5429.851.
47. Giuliani, A.D.G. Pearson kimberlites: From deep earth to diamond mines. *Elements* **2019**, *15*, 377–380, doi:https://doi.org/10.2138/gselements.15.6.377.